available at www.sciencedirect.com

ScienceDirect

journal homepage: www.elsevier.com/locate/chnjc

Article

Photocatalytic removal of nitric oxide by multi-walled carbon nanotubes-supported TiO_2

Hao Liu [a], Hairu Zhang [b], Hongmin Yang [a,*]

[a] *School of Energy and Mechanical Engineering, Nanjing Normal University, Nanjing 210042, Jiangsu, China*
[b] *Design Institute of Nanjing Shengnuo Heat Pipe Co., Ltd, Nanjing 210009, Jiangsu, China*

ARTICLE INFO

Article history:
Received 21 July 2013
Accepted 5 September 2013
Published 20 January 2014

Keywords:
Multi-walled carbon nanotube
Titanium dioxide
Photocatalysis
Denitration
Flue gas

ABSTRACT

Multi-walled carbon nanotubes (MWCNTs) coated with TiO_2 were prepared by a sol-gel method and characterized by transmission electron microscopy, X-ray photoelectron spectroscopy, X-ray diffraction, and UV-Vis diffuse reflectance spectroscopy. It was found that MWCNTs/TiO_2 consisted mainly of anatase phase. The introduction of MWCNTs inhibited TiO_2 grain growth. Moreover, the adsorption edge of MWCNTs/TiO_2 shifted toward long-wavelength region compared with bare TiO_2. The photocatalytic ability of MWCNTs/TiO_2 for NO removal was experimentally investigated in a fixed-bed reactor. The results showed that a lower initial NO concentration was conducive to NO removal. A negative effect of SO_2 on denitration was observed. In contrast, O_2 and H_2O played a promotional role in the photocatalytic denitration. At optimal conditions (73 mg/m^3 NO, 8% O_2, 5% H_2O), NO removal efficiency of 46% was achieved. In addition, the reaction mechanism of denitration was proposed.

1. Introduction

The major sources of NO are coal power plants and the combustion of fossil fuels in automobiles. Acid rain and photochemical fog caused by NO emission have led to great harm to environment and human health [1,2]. Most coal-fired power plants are equipped with selective catalytic reduction (SCR) systems or selective non-catalytic reduction (SNCR) systems to control NO emission. Although SCR performs effectively in NO reduction, problems such as the expense of operating the catalytic system and catalyst poisoning need to be tackled. Although NO is decomposed without a catalyst in the case of SNCR, practical constraints including the temperature window and time lead to worse NO removal efficiency [3–5]. Photocatalytic technology has received wide-ranging attention as a promising way to remove the various toxic pollutants in flue gas. TiO_2 has been widely applied due to its stability, nontoxicity, and high photocatalytic reactivity [6]. Wang et al. [7] used TiO_2 loaded on woven glass fabric to remove nitrogen oxides by photocatalytic oxidation. Zhao et al. [8] studied the photocatalytic oxidation of NO with supported nano-TiO_2. However, low removal efficiencies are achieved in practice by TiO_2 due to its wide energy band gap (3.2 eV) and easy recombination of electron-hole pairs. Many studies have emphasized the modification of TiO_2 to increase yields of radicals and shift the adsorption edges toward the visible light region. N-doped TiO_2 prepared by Ananpattarachai et al. [9] and B-doped TiO_2 synthesized by Li et al. [10] revealed that the introduction of dopants can reduce the band gap of TiO_2. Li et al. [11] reported that Cu-tetracarboxyphthalocyanine sensitized mesoporous TiO_2

* Corresponding author. Tel: +86-25-85481132; Fax: +86-25-85481273; E-mail: yanghongmin@njnu.edu.cn
This work was supported by the National Natural Science Foundation of China (50976049), the Natural Science Foundation of Jiangsu (BK2011788) and Research Innovation Program for College Graduates of Jiangsu Province (CXLX12-0410).
DOI: 10.1016/S1872-2067(12)60705-0 | http://www.sciencedirect.com/science/journal/18722067 | Chin. J. Catal., Vol. 35, No. 1, January 2014

performed effectively under visible light. Multi-walled carbon nanotubes (MWCNTs) have also been the focus of considerable numbers of studies because of their excellent mechanical, electrical, thermal, and magnetic properties [12]. Wang et al. [13] synthesized MWCNTs-TiO_2 using a sol-gel method and evaluated their photocatalytic ability by phenol decomposition. Yang et al. [14] used CNT-TiO_2 synthesized by a hydrothermal method to decompose methyl orange. In previous investigations, the main concerns of most studies focused on MWCNTs/TiO_2 have been mostly to do with their physicochemical properties and the photocatalytic reaction mechanism. The photocatalytic abilities of these materials were evaluated by the decomposition of dyes, phenol, etc. Seldom has research focused on the photocatalytic removal of NO from flue gas by MWCNTs/TiO_2 been reported.

In this paper, MWCNTs/TiO_2 was synthesized by a sol-gel method and characterized by transmission electron microscopy (TEM), X-ray photoelectron spectroscopy (XPS), X-ray diffraction (XRD), and ultraviolet-visible (UV-Vis) diffuse reflectance spectroscopy to give insight into its physicochemical properties. Systematic photocatalytic NO removal experiments were conducted for the first time. Influencing factors (O_2, H_2O, SO_2, and NO) and the effect of the MWCNTs on the NO removal were studied, and a possible reaction mechanism for the denitration was proposed.

2. Experimental

2.1. Preparation of MWCNTs/TiO_2

Raw MWCNTs were purchased from Chengdu Organic Chemicals Company (purity > 95%, diameter 10–20 nm, length 10–30 μm). The raw MWCNTs were acid-treated and functionalized in a mixture of concentrated sulphuric acid and nitric acid (Nanjing Chemical Reagent Company, Nanjing, China) in a volume ratio of 3:1. The acid-treated MWCNTs were rinsed with distilled water until they reached neutral pH and were then dried at 80 °C for 12 h.

MWCNTs/TiO_2 was synthesized by a sol-gel method. In a typical synthesis, a certain amount of acid-treated MWCNTs was sonicated in a solution containing 75 mL anhydrous ethanol (AR, Nanjing Chemical Reagent Company, Nanjing, China), 25 mL tetrabutyl titanate (AR, Nanjing Chemical Reagent Company, Nanjing, China), and 4 mL HNO_3 under vigorous stirring. After stirring for 1 h, a mixture of 25 mL anhydrous ethanol and 5 mL distilled water (the PH was adjusted to about 2) was added dropwise to the solution. The resultant gel was dried at 80 °C and then calcined at 350–650 °C in air for 3 h. Bare TiO_2 was used as a control sample, following similar preparation steps to those mentioned above. To avoid aggregation of the photocatalysts above the quartz air distributor, all tested photocatalysts were loaded on heat-pretreated silica gel having a diameter of 2 cm. The loading method was detailed in the work of Sannino et al. [15].

2.2. Characterization of MWCNTs/TiO_2

The bare TiO_2 and composites were characterized using a range of analytical techniques. TEM observations were made with a JEOL JEM-2100F microscope at 200 kV. Samples for imaging were sonicated in anhydrous ethanol and collected on a copper carbon-coated TEM grid. The chemical compositions of the MWCNTs/TiO_2 were studied by XPS using a PHI Quantera. XRD was performed to characterize the phase composition and crystal structure of the photocatalysts using a Rigaku D/max-2500/PC X-ray diffractometer with Cu K_α radiation from 5° to 85° at a scanning speed of 0.02°/s. The UV-Vis diffuse reflectance spectra of the composites were measured on a VARIAN Cary 5000 spectrophotometer.

2.3. Photocatalyst test

The schematic of the experimental system is shown in Fig. 1. The experiments were conducted in a fixed-bed photoreactor

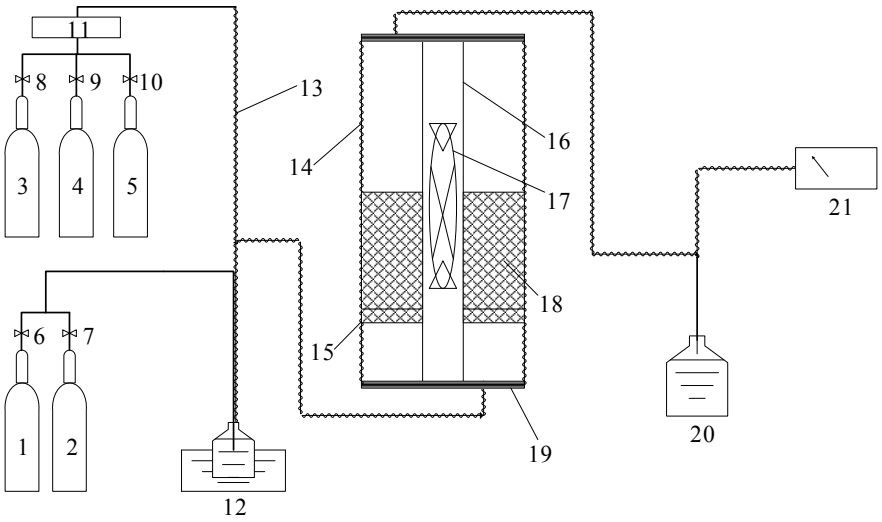

Fig. 1. Schematic diagram of the photoreactor system. 1,3–N_2 gas cylinders; 2–O_2 gas cylinders; 4–NO gas cylinders; 5–SO_2 gas cylinders; 6,7,8,9,10–Mass flow meters; 12–Water bubbler; 13–Heating belts; 14–Outer tube; 15–Quartz air distributor; 16–Inner tube; 17–High pressure mercury lamp; 18–Photocatalysts; 19–Rubber plug; 20–Absorption chamber; 21–Flue gas analyzer.

comprised of 60 cm-long double concentric quartz tubes. The diameters of the inner and outer tubes were 28 and 60 mm, respectively. A 125 W high pressure mercury lamp (Shanghai Jiguang Lighting Company, Shanghai, China) was placed vertically in the inner tube as the UV source. The intensity provided by the lamp was 6.5 W/m^2 at the peak wavelength of 365 nm. The composition of the simulated flue gases was 0–8% O_2, 0–15% H_2O, 73–508 mg/m^3 NO, 155–1241 mg/m^3 SO_2, and N_2 as balance. O_2, SO_2, NO, and N_2 were supplied from gas cylinders, and the flow rates of the different gases were controlled by a mass flow meter (Beijing Metron Instrument Company, Beijing, China). The N_2 flow was divided into two streams. One stream combined with O_2 and was allowed to pass through a water bubbler to set the desired water vapor level. The second stream was converged with NO. The total flow rate remained constant at 2 L/min and a space velocity of 250 h^{-1}. An ECOM–J2KN (RBR Company, German) was situated downstream to the fixed-bed photoreactor to record the concentration of NO in real time. Adsorption equilibrium of the photocatalysts was achieved by introducing NO into the system before switching on the UV light. The reaction time was set to 15 min for each experiment. NO removal efficiency could be defined as $R_{NO} = [(NO_{in} - NO_{out})/NO_{in}] \times 100\%$, where NO_{in} and NO_{out} represent the NO in the inlet and outlet of the photochemical reactor, respectively.

The experimental conditions are listed in Table 1. To examine the reaction mechanism involved in the photocatalytic removal of NO, Case 1 was conducted to investigate the adsorption of NO on MWCNTs/TiO_2. In Case 2, photocatalytic denitration was conducted under different conditions (UV, Silica gel, TiO_2, MWCNTs/TiO_2). Cases 3–6 were carried out to study the effects of NO, O_2, H_2O, and SO_2 on NO removal. The amount of photocatalysts used in photocatalytic denitration was 25 g.

3. Results and discussion

3.1. Morphology

Figure 2 shows TEM images of MWCNTs and MWCNTs/TiO_2. It was found in Fig. 2(a) that the aggregation of the MWCNTs as well as amorphous carbon and impurities on the surface of the MWCNTs. The external diameter of the raw MWCNTs was 15–30 nm. Figure 2(b) shows the typical hollow structures of MWCNTs. After acid-treatment, opening of the tube ends and breakage of the tubes were also observed. For MWCNTs/TiO_2 sample (Fig. 2(c)), MWCNTs were wrapped with TiO_2 having an external diameter larger than 20 nm, confirming tight connection between them.

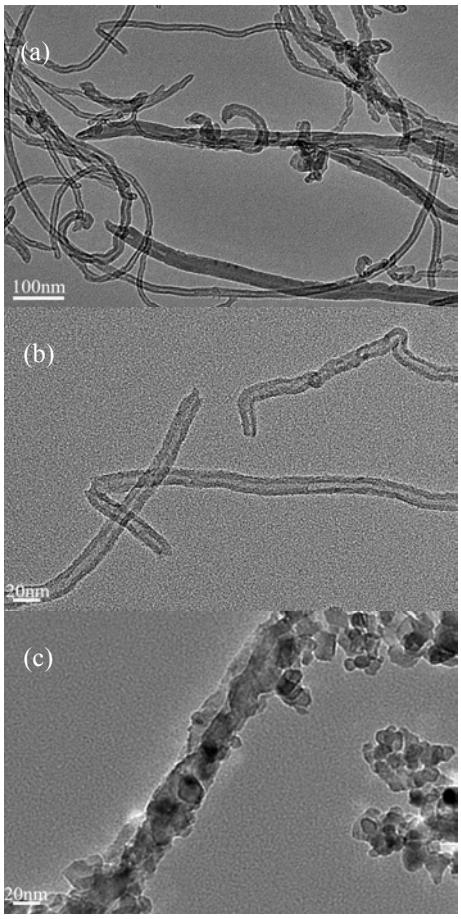

Fig. 2. TEM images of raw MWCNTs (a), acid-treated MWCNTs (b), and MWCNTs/TiO_2 (c) samples.

3.2. Crystalline phase characterization

Figure 3 shows the XRD patterns of MWCNTs/TiO_2 calcined at different temperatures. MWCNTs/TiO_2 calcined at 350 and 500 °C consisted mainly of anatase phase, and the typical diffraction peaks were found at 25.1°, 36.9°, 37.6°, 38.5°, 47.9°, 53.8°, 55.0°, 62.6°, and 75.1°, corresponding to the reflections from (101), (103), (004), (112), (200), (105), (211), (204), and (215) crystal planes, respectively, of the anatase phase. The full width at half maximum of (101) for MWCNTs/TiO_2 calcined at 500 °C was shorter than that calcined at 350 °C, indicating an increase in crystallinity. Significant phase transformation was induced by heat-treatment at 650 °C. The anatase phase transformed mostly to the rutile phase, indicated by the typical rutile diffraction peak observed at 27.4°. Moreover, the weight of samples calcined at 650 °C as measured by analytical balance

Table 1
Experimental conditions for photocatalytic removal of NO.

Case	O_2 (%)	H_2O (%)	NO (mg/m^3)	SO_2 (mg/m^3)	Material	UV light
1	8	5	181	—	MWCNTs/TiO_2	off
2	8	5	73	—	Silica gel, TiO_2, MWCNTs/TiO_2	on
3	8	5	73/181/254/508	—	MWCNTs/TiO_2	on
4	0/3/6/8	5	73	—	MWCNTs/TiO_2	on
5	8	0/1/5/15	73	—	MWCNTs/TiO_2	on
6	8	5	73	155/310/620/1241	MWCNTs/TiO_2	on

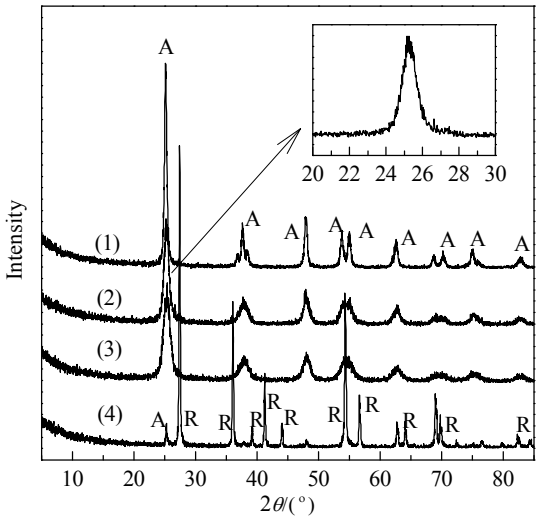

Fig. 3. XRD patterns of MWCNTs/TiO_2 calcined at different temperatures. (1) TiO_2, 500 °C; (2) MWCNTs/TiO_2, 350 °C; (3) MWCNTs/TiO_2, 500 °C; (4) MWCNTs/TiO_2, 650 °C.

(AUX320, SHIMADZU, Japan) decreased significantly compared with that of samples heat-treated at 500 °C (the weight of sample heat-treated at 500 °C was approximate to the theoretical value during preparation), revealing that heat-treatment at 650 °C led to MWCNTs oxidation loss. Li et al. [16] also confirmed a significant weight loss for MWCNTs at 550–750 °C in TGA experiments. Contaminant phases were not observed during XRD analysis. Cong et al. [17] reported that the (002) reflection of MWCNTs was overlapped by (101) of TiO_2 due to their proximity at 26.3° and 25.3°, respectively. No diffraction peak from the MWCNTs was found after peak fitting at 20°–30°, and the absent (002) reflection was attributed to the low content and uniform dispersion of the MWCNTs. The (101) peak of MWCNTs/TiO_2 calcined at 500 °C was broadened compared with that of bare TiO_2, which correlated closely with the decreased crystallite size. Scherrer's formula was used to give an approximate calculation of crystallite size based on the FWHM of the (101) peak. The crystallite sizes of TiO_2 and MWCNTs/TiO_2 calcined at 500 °C were thereby found to be 19.1 and 11 nm, respectively, suggesting that the MWCNTs inhibited the grain growth of TiO_2 during crystallization. The average TiO_2 particle size estimated from the TEM images was about 15 nm, larger than that calculated from XRD. According to Lin et al. [18], a larger TEM estimated size is attributable to the aggregation of TiO_2 nanoparticles into larger particles, while XRD calculates the size of single crystallites. MWCNTs/TiO_2 calcined at 500 °C was used for photocatalyst test.

3.3. XPS analysis

Figure 4(a) shows XPS spectrum of MWCNTs/TiO_2 and clearly reveals that the main elements on the sample surface were Ti, C, and O. Figure 4(b) displays the C 1*s* spectra of the MWCNTs/TiO_2 sample. Three peaks were observed in the C 1*s* spectra after peak fitting. The main peak was located at 284.6 eV, ascribed to graphitic carbon and C–C bonds from MWCNTs. The second at 285.9 eV was attributed to C–O bonds, and the broad peak located at 287.9 eV represented C=O and COO bonds [17]. Figure 4(c) shows the O1s spectra of the sample, which was fitted into three peaks. The O 1*s* peak at 530.1 eV corresponded to lattice oxygen, while the higher binding ener-

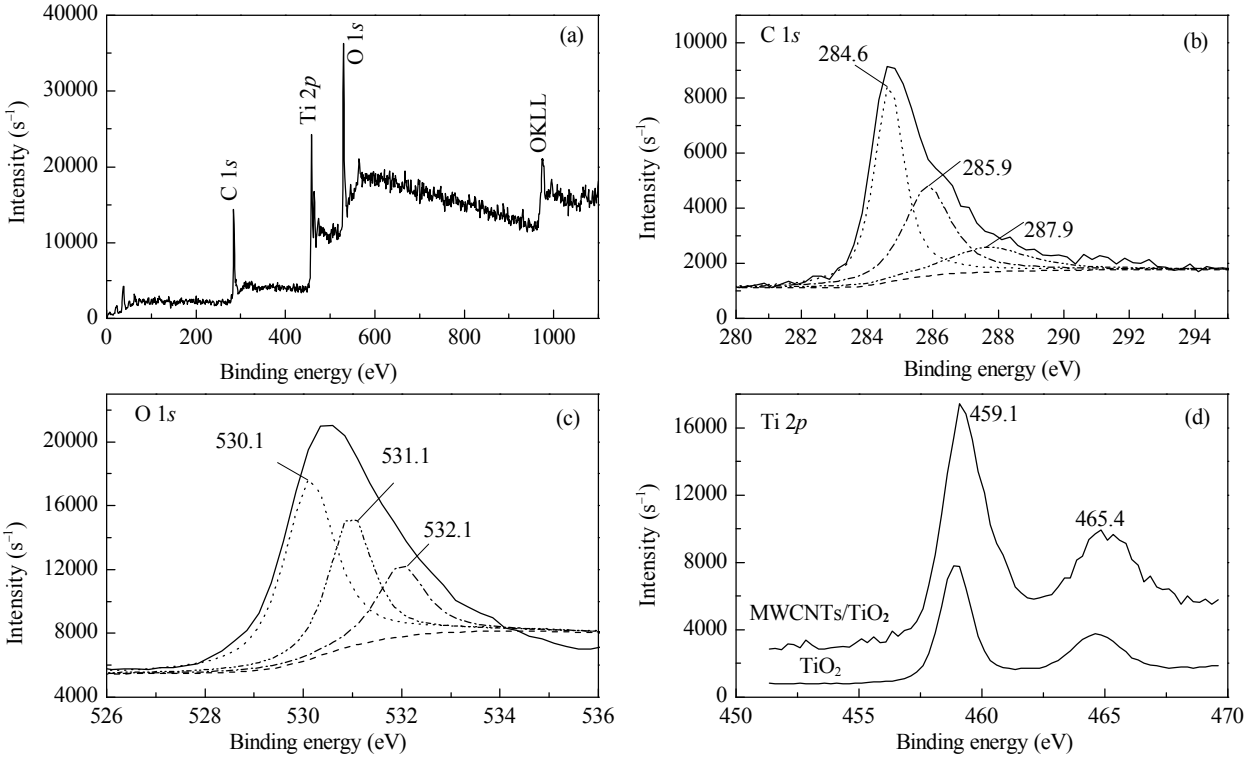

Fig. 4. XPS spectra of MWCNTs/TiO_2 sample. (a) General XPS spectrum; (b–d) XPS spectra of C 1*s*, O 1*s*, and Ti 2*p*.

gies of 531.1 and 532.1 eV were assigned to surface hydroxyl oxygen and C–O bonds, respectively [17,19]. Obviously, Ti–O and C–O bonds present in the C 1*s* and O 1*s* XPS spectra after peak fitting led to the anticipation of intimate connection between MWCNTs and TiO_2 through Ti–O–C bonds. Figure 4(d) reveals the Ti ($2p_{3/2}$, $2p_{1/2}$) spectra. The binding energies of Ti $2p_{3/2}$ and Ti $2p_{1/2}$ were 459.1 and 465.4 eV, respectively, indicating the typical presence of Ti^{4+} in the TiO_2. Moreover, increases in the binding energies of Ti 2*p* compared with that of bare TiO_2 were observed and assigned to electrons transferring through Ti–O–C bonds changing the electron density of Ti^{4+} in TiO_2.

3.4. Optical properties

The UV-Vis DRS spectra of MWCNTs/TiO_2 and TiO_2 are presented in Fig. 5(a). TiO_2 showed a typical adsorption edge at about 400 nm and weak absorption in the visible light region. In contrast, a positive effect could be observed in the presence of MWCNTs; the absorption edge was red-shifted toward the long wavelength region. This shift suggested a decrease in the Fermi level induced by electron transfer through Ti–O–C bonds [20]. Moreover, the MWCNTs/TiO_2 composite exhibited enhanced visible-light-absorption efficiency compared with that of bare TiO_2, which was attributed to the possible electronic transition $\pi \rightarrow \pi^*$ in the MWCNTs and the black color of the photocatalysts [21]. Figure 5(b) shows a plot of $[F(R)h\nu]^{1/2}$ versus photo energy. The extrapolation of $[F(R)h\nu]^{1/2}$ to the abscissa at zero $F(R)$ provided the band gap energies of MWCNTs/TiO_2 and TiO_2 to be 2.6 and 3.0 eV, respectively, confirming the narrowed band gap energy of MWCNTs/TiO_2.

3.5. Photocatalytic denitration

3.5.1. Baseline experiments

Figure 6 reveals the NO adsorption ability of MWCNTs/TiO_2. To measure the NO adsorption of the photocatalyst, NO was first introduced into the bypass and maintained steadily at 189 mg/m^3. The bypass valve was then shut, and NO was introduced into the reactor, which contained the photocatalyst. The NO concentration decreased sharply at first and reached a minimum of 162 mg/m^3 after 3 min. The NO concentration

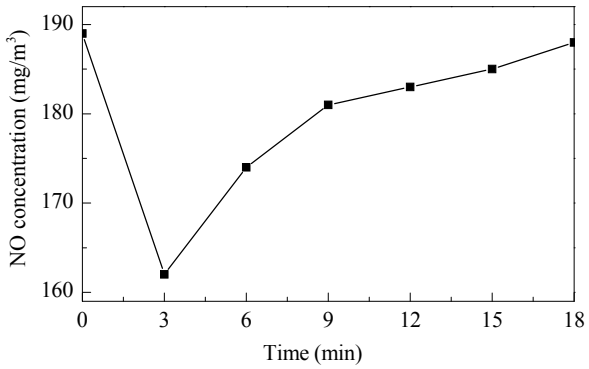

Fig. 6. NO adsorption performance of MWCNTs/TiO_2 loaded on silica gel.

then started to increase and reached its original level after 18 min. The maximum NO adsorption efficiency was 14%.

Figure 7 shows the results of photocatalytic denitration conducted under different conditions (UV, silica gel, TiO_2, MWCNTs/TiO_2). Some NO reaction occurred under UV irradiation even in the absence of photocatalyst, and R_{NO} was about 16%. The reaction mechanism for NO removal was similar to that for formation of photochemical smog. Active O formed by NO_2 photolysis and O_3 formed by O reacting with O_2 were able to oxidize NO to higher valence state. The reaction mechanism [22] induced by UV irradiation can be defined by reactions (1)–(6):

$$NO_2 + h\nu \rightarrow NO + O \quad (1)$$

$$O + O_2 \rightarrow O_3 + O + M \quad (2)$$

$$O_3 + NO \rightarrow NO_2 + O_2 \quad (3)$$

$$O + NO + M \rightarrow NO_2 + M \quad (4)$$

$$O + NO_2 + M \rightarrow NO_3 + M \quad (5)$$

$$O_3 + NO_2 + M \rightarrow NO_3 + O_2 + M \quad (6)$$

To increase the interfacial area for vapor-solid contact and reaction time, MWCNTs/TiO_2 was loaded onto silica gel for the photocatalytic experiments. It was therefore necessary to investigate the role of silica gel in photocatalytic denitration. Figure 7 indicates that no remarkable NO reaction was observed on the silica gel. However, R_{NO} decreased slightly compared with the case without photocatalyst. This decrease in R_{NO} was expected to result from photon energy loss caused by refraction and reflection of UV light by the silica gel. In denitration

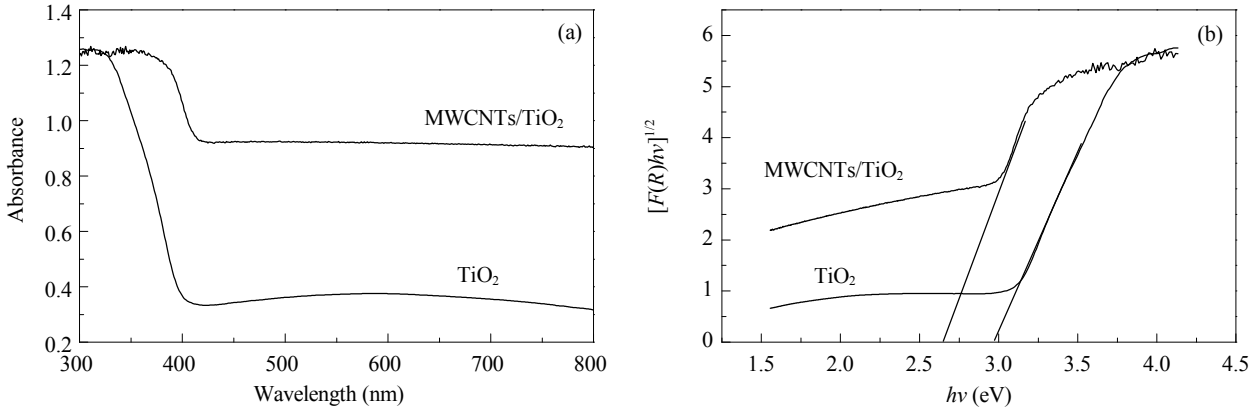

Fig. 5. (a) DRS spectra of MWCNTs/TiO_2 and TiO_2; (b) Plot of $[F(R)h\nu]^{1/2}$ vs photon energy of TiO_2 and MWCNTs/TiO_2.

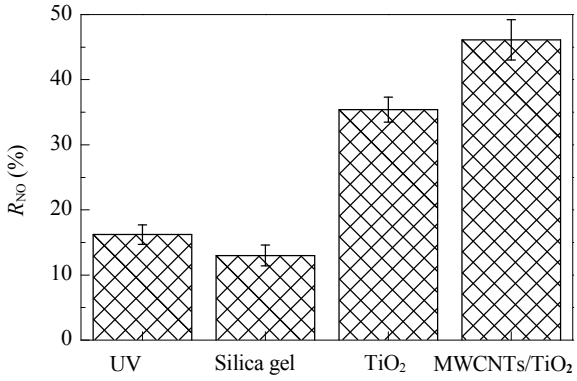

Fig. 7. Effect of UV and various types of photocatalysts on NO removal.

experiments, the effect of the silica gel on R_{NO} was negligible.

Compared with the case without photocatalyst, MWCNTs/TiO_2 and TiO_2 performed well in photocatalytic denitration, the R_{NO} of which reached 46% and 35% respectively. The results revealed that the process of photocatalytic NO removal was more effective than the photochemical NO removal process. In the presence of photocatalyst, the incident UV radiation ejected electrons from the valence band of the photocatalyst to the conduction band. The photogenerated electrons and holes formed diffused toward the photocatalyst surface. Once the photoinduced electrons and holes have been trapped by surface adsorbed species like O_2 and H_2O, active O_2^- and ·OH were formed and were capable of oxidizing NO to NO_2, HNO_2, or HNO_3. It was reported by Devahasdin et al. [23] that NO oxidation involves the following series of steps: NO → HNO_2 → NO_2 → HNO_3. In the initial stage, HNO_2 was the dominating reaction product. Once the photocatalysts were saturated with HNO_3, NO_2 to HNO_3 conversion was inhibited, and the reaction only went as far as NO_2. The reaction mechanism [23,24] for NO removal in the presence of photocatalyst can be defined by reactions (7)–(13):

$$TiO_2 + h\nu \rightarrow e^- + h^+ \quad (7)$$

$$h^+ + OH^- \rightarrow \cdot OH \quad (8)$$

$$e^- + O_2 \rightarrow O_2^- \quad (9)$$

$$NO + \cdot OH \rightarrow HNO_2 \quad (10)$$

$$HNO_2 + \cdot OH \rightarrow NO_2 \quad (11)$$

$$NO_2 + \cdot OH \rightarrow NO_3^- \quad (12)$$

$$NO + O_2^- \rightarrow NO_3^- \quad (13)$$

3.5.2. The effect of MWCNT

As shown in Fig. 7, a positive effect of MWCNTs on NO removal was observed; 46% of R_{NO} was achieved on MWCNTs/TiO_2 compared with 35% of R_{NO} on bare TiO_2. This enhancement could be attributed to the following three aspects. The first is good conductivity of MWCNTs. Considering the limited pathways for electron transfer in bare TiO_2, the MWCNTs provided alternative pathways for electrons to transfer through Ti–O–C bonds, prolonging electron-hole pair lifetimes [25,26]. The second is the smaller crystallite size of MWCNTs/TiO_2. XRD analysis confirmed that introducing MWCNTs inhibited the grain growth of the TiO_2. Devi et al. [27] suggested that volume recombination dominated the possible ways for electron-hole recombination. Large crystallite sizes, which result in longer diffusion path length, allowed more chance for electron-hole recombination. Hence, smaller crystallite size favors the diffusion of more electrons and holes to the surface. The third is the narrow band gap energy of MWCNTs/TiO_2. In DRS analysis, the adsorption edge of MWCNTs/TiO_2 was found to be shifted toward longer wavelengths compared with that of bare TiO_2. It was expected that more electron-hole pairs were created at the same UV intensity as a result of this red shift.

3.5.3. The effect of gas components

Figure 8(a) underlines the effect of NO initial concentration on NO removal. R_{NO} decreased sharply at first and then leveled off with increasing NO. These results indicated that a lower initial NO concentration was conducive to NO removal. The behavior depicted in Fig. 8(a) revealed that the NO removal reaction was ruled by the Langmiur-Hinshelwood model, namely first-order reaction at low concentration and zero-order reaction at high concentration [7]. Because a great deal of SO_2 is emitted from power plants during the combustion of coal, it was necessary to investigate the effect of SO_2 on NO removal. As shown in Fig. 8(b), R_{NO} declined sharply to 39% when 155 mg/m^3 SO_2 was introduced into the system and further declined to 29% at 1241 mg/m^3 SO_2, a remarkable decrease compared with the initial value of R_{NO} in the absence of SO_2. The decrease in R_{NO} under complex gas atmosphere was attributed to SO_2 and NO competing for the limited adsorption and reaction sites. Li et al. [28] reported that surface hydroxyl groups are the dominant adsorption sites for NO, while surface

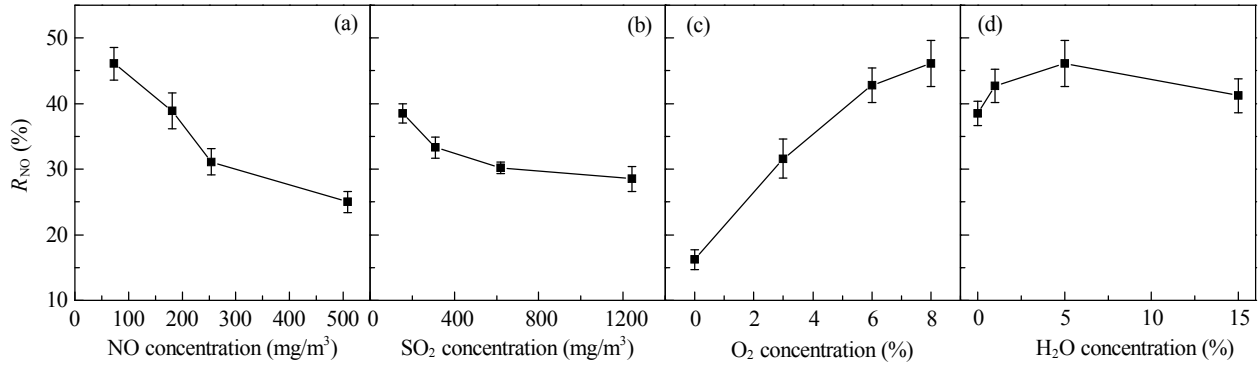

Fig. 8. Effect of initial NO (a), SO_2 (b), O_2 (c), and H_2O (d) concentrations on NO removal Efficiency (R_{NO}).

hydroxyl groups and lattice oxygen are responsible for adsorption of SO_2 [29]. A lower R_{NO} was therefore as a result of SO_2 and NO competing for the limited surface hydroxyl groups.

Many studies have suggested positive effects of O_2 and H_2O on photocatalytic oxidation. Figure 8(c) reveals the effect of O_2 on NO removal. R_{NO} was as low as 17% in the absence of O_2 but increased to 46% at an O_2 content of 8%. Figure 8(d) shows the effect of H_2O on NO removal. R_{NO} increased to a maximum value of 46% at 5% H_2O and then decreased to 41% at 15% H_2O. These results indicated that suitable concentrations of O_2 and H_2O played a prominent role in NO removal. Photoinduced electrons and holes were scavenged by O_2 and surface hydroxyl groups to form O_2^- and ·OH (reactions (8) and (9)), which improved reactions (10)–(13) [30]. Hence, the observed enhancement of R_{NO} was justified. However, more studies have focused on studying the effect of H_2O than that of O_2 due to the high activity of ·OH and the both inhibiting and promoting role that H_2O plays in photocatalytic oxidation. H_2O plays an important role in the formation of surface hydroxyl groups, which not only acted as adsorption sites for O_2 and NO, but also for H_2O through hydrogen bonding. R_{NO} was enhanced due to the greater amount of hydroxyl groups formed [31]. Zhao et al. [8] observed a negative effect of H_2O on NO removal at H_2O content greater than 6%, but they did not give a cause for the decrease in R_{NO}. However, Henderson [32] revealed that water layers formed outside the photocatalyst were capable of blocking the diffusion of target molecules toward adsorption and reaction sites, and that O_2 was also blocked by water layers, inhibiting the formation of O_2^-. In this paper, a positive role of H_2O was found in an H_2O concentration range of 0–5%, while an inhibitory effect was observed at 15%, revealing that a water layer may have formed outside the photocatalyst and blocked the diffusion of the target molecule. In addition, H_2O has an effect on the migration of the reaction products of photocatalytic denitration, which prevents photocatalyst deactivation [33,34]. Typically, HNO_2 and HNO_3 are deposited on the TiO_2 surface during the NO removal reaction and block the absorption sites of TiO_2 for further NO conversion, and thus deactivation occurs. In the presence of H_2O, adsorbed photocatalytic products, including adsorbed HNO_2 and HNO_3, are converted into water soluble products, and H_2O thereby assists in the self-cleaning of photocatalysts.

4. Conclusions

MWCNTs/TiO_2 was successfully synthesized using a sol-gel method. The introduction of MWCNTs refined the physical and chemical structure. The decreased crystallite size of MWCNTs/TiO_2 lowered the chance for volume recombination. Moreover, MWCNTs provided alternative electrons transfer pathway to assist in hole-electron pairs separation. These aspects contributed to better denitration performance on MWCNTs/TiO_2 compared to bare TiO_2. In the study of photocatalytic denitration, at optimal conditions (73 mg/m^3 NO, 8% O_2, 5% H_2O), an optimal denitration efficiency of 46% was observed on MWCNTs/TiO_2. A lower NO initial concentration was found to be conducive to NO removal. However, R_{NO} was lower in the presence of SO_2, because SO_2 and NO competed for limited adsorption and reaction sites. O_2 and H_2O were found to play promotional roles in NO removal due to the formation of active O_2^- and ·OH species. For excess H_2O, a water layer may formed outside the photocatalyst to inhibit photocatalytic denitration, and the negative effect of excess H_2O (15%) on NO removal was observed.

References

[1] Liang Z Y, Ma X Q, Lin H, Tang Y T. *Appl Energy*, 2011, 88: 1120
[2] Sun W Y, Ding S L, Zeng S S, Su S J, Jiang W J. *J Hazard Mater*, 2011, 192: 124
[3] Nguyen T D B, Lim Y I, Eom W H, Kim S J, Yoo K S. *Comput Chem Eng*, 2010, 34: 1580
[4] Bae S W, Roh S A, Kim S D. *Chemosphere*, 2006, 65: 170
[5] Roy S, Hegde M S, Madras G. *Appl Energy*, 2009, 86: 2283
[6] Maggos Th, Bartzis J G, Liakou M, Gobin C. *J Hazard Mater*, 2007, 146: 668
[7] Wang H Q, Wu Z B, Zhao W R, Guan B H. *Chemosphere*, 2007, 66: 185
[8] Zhao L, Zhao Y, Han J, Song L Q. *Acta Chim Sin* (赵莉, 赵毅, 韩静, 宋立琴. 化学学报), 2008, 66: 2001
[9] Ananpattarachai J, Kajitvichyanukul P, Seraphin S. *J Hazard Mater*, 2009, 168: 253
[10] Li L, Yang Y L, Liu X R, Fan R Q, Shi Y, Li S, Zhang L Y, Fan X, Tang P X, Xu R, Zhang W Z, Wang Y Z, Ma L Q. *Appl Surf Sci*, 2013, 265: 36
[11] Li X P, Chen F, Zhang J L. *Chin J Catal* (李晓佩, 陈锋, 张金龙. 催化学报), 2007, 28: 229
[12] Paradise M, Goswami T. *Mater Des*, 2007, 28: 1477
[13] Wang W D, Serp P, Kalck P, Silva C G, Faria J L. *Mater Res Bull*, 2008, 43: 958
[14] Yang H P, Shi Z M, Dai K J, Wu J M. *Acta Chim Sin* (杨汉培, 石泽敏, 戴开静, 段云平, 吴俊明. 化学学报), 2011, 69: 536
[15] Sannino D, Vaiano V, Ciambelli P, Eloy P, Gaigneaux E M. *Appl Catal A*, 2011, 394: 71
[16] Li Z Y, Gao B, Chen G Z, Mokaya R, Sotiropoulos S, Puma G L. *Appl Catal B*, 2011, 110: 50
[17] Cong Y, Li X K, Qin Y, Dong Z J, Yuan G M, Cui Z W, Lai X J. *Appl Catal B*, 2011, 107: 128
[18] Lin X X, Rong F, Fu D G, Yuan C W. *Powder Technol*, 2012, 219: 173
[19] Xin B F, Wang P, Ding D D, Liu J, Ren Z Y, Fu H G. *Appl Surf Sci*, 2008, 254: 2569
[20] Cong Y, Qin Y, Li X K, Dong Z J, Yuan G M, Cui Z W. *Acta Phys-Chim Sin* (丛野, 秦云, 李轩科, 董志军, 袁观明, 崔正威. 物理化学学报), 2011, 27: 1509
[21] Ou Y, Lin J D, Fang S M, Liao D W. *Chem Phys Lett*, 2006, 429: 199
[22] Smith J P, Urone P. *Environ Sci Technol*, 1974, 8: 742
[23] Devahasdin S, Fan C Jr, Li K, Chen D H. *J Photochem Photobiol A*, 2003, 156: 161
[24] Yuan Y, Zhang J Y, Li H L, Li Y, Zhao Y C, Zheng C G. *Chem Eng J*, 2012, 192: 21
[25] Kuo C Y. *J Hazard Mater*, 2009, 163: 239
[26] Kongkanand A, Domínguez R M, Kamat P V. *Nano Lett*, 2007, 7: 676
[27] Devi L G, Murthy B N, Kumar S G. *Mater Sci Eng B*, 2010, 166: 1
[28] Li S C, Jacobson P, Zhao S L, Gong X Q, Diebold U. *J Phys Chem C*, 2012, 116: 1887
[29] Baltrusaitis J, Jayaweera P M, Grassian V H. *J Phys Chem C*, 2010, 115: 492
[30] Lu S Y, Wang Q L, Buekens A G, Yan J H, Li X D, Cen K F. *Chem Eng J*,

Graphical Abstract

Chin. J. Catal., 2014, 35: 66–77 doi: 10.1016/S1872-2067(12)60705-0

Photocatalytic removal of nitric oxide by multi-walled carbon nanotubes-supported TiO_2

Hao Liu, Hairu Zhang, Hongmin Yang*
Nanjing Normal University;
Design Institute of Nanjing Shengnuo Heat Pipe Co., Ltd

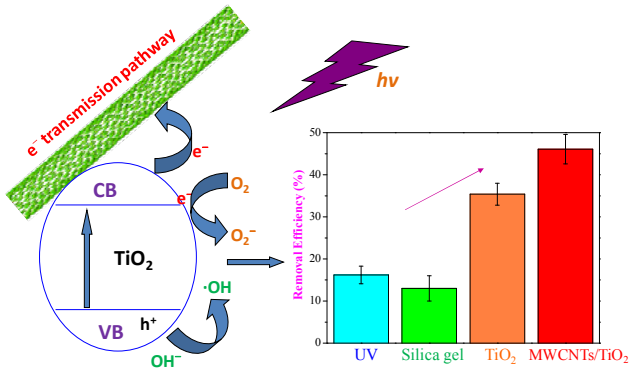

MWCNTs provide another transfer pathway for photogenerated electrons, assisting in electron and hole separation. This electron-scavenging character of MWCNTs causes MWCNTs/TiO_2 to perform better in photocatalytic denitration than bare TiO_2.

2012, 195-196: 233
[31] Wendt S, Matthiesen J, Schaub R, Vestergaard E K, Lagsgaard E, Besenbacher F, Hammar B. *Phys Rev Lett*, 2006, 96: 066107
[32] Henderson M A. *Surf Sci Rep*, 2011, 66: 185
[33] Miller T M, Grassian V H. *Geophys Res Lett*, 1998, 25: 3835
[34] Guan K S. *Surf Coat Technol*, 2005, 191: 155

多壁碳纳米管负载TiO_2的光催化脱硝性能

刘 浩[a], 张海茹[b], 杨宏旻[a,*]
[a]南京师范大学能源与机械工程学院, 江苏南京210042
[b]南京圣诺热管有限公司设计院, 江苏南京210009

摘要: 采用溶胶凝胶法制备了多壁碳纳米管负载TiO_2 (MWCNTs/TiO_2), 并利用透射电镜、X射线光电子能谱、X射线衍射和紫外-可见漫反射光谱对样品进行了表征. 结果表明, MWCNTs/TiO_2晶型以锐钛矿为主, MWCNTs的引入会限制TiO_2晶粒的生长. 另外, MWCNTs/TiO_2的光吸收边向长波区域偏移. 针对模拟烟气, 在固定床光催化反应器中对采用涂覆处理的MWCNTs/TiO_2的光催化脱硝性能进行了实验研究. 结果表明, NO初始浓度较低时, 光催化脱硝效率较高, SO_2的存在可抑制光催化脱硝过程, 而O_2及H_2O则有促进作用. 在最佳实验条件(73 mg/m^3 NO, 8% O_2, 5% H_2O)下, 光催化脱硝效率可达46%. 提出了光催化脱硝反应机理.

关键词: 多壁碳纳米管; 二氧化钛; 光催化; 脱硝; 烟气

收稿日期: 2013-07-21. 接受日期: 2013-09-05. 出版日期: 2014-01-20.
*通讯联系人. 电话: (025) 85481132; 传真: (025) 85481273; 电子信箱: yanghongmin@njnu.edu.cn
基金来源: 国家自然科学基金(50976049); 江苏省自然科学基金(BK2011788); 江苏省研究生科研创新计划(CXLX12-0410).
本文的英文电子版由Elsevier出版社在ScienceDirect上出版(http://www.sciencedirect.com/science/journal/18722067).

1. 前言

大气中NO_x主要源于燃煤电站以及机动车尾气的排放, 是形成酸雨及光化学烟雾的诱因之一. NO排放的加剧严重危害了生态环境及人类健康状况[1,2]. 目前, 燃煤电站氮氧化物脱除技术以选择性催化还原(SCR)及选择性非催化还原(SNCR)为主. SCR具有较高的脱硝效率, 但存在投资成本较高及催化剂毒化等问题; 而SNCR无需使用催化剂, 但温度窗口及反应时间等不易控制, 导致脱硝效率较低[3–5]. 作为一种新的大气污染控制技术, 以无毒无害的TiO_2为基础的光催化氧化法受到广泛的关注[6]. Wang等[7]利用玻璃纤维负载TiO_2, 在固定床反应器中进行NO的光催化氧化实验. 赵莉等[8]利用石英砂负载的TiO_2对NO进行光催化脱除. 在实际应用过程中, TiO_2存在禁带宽度大(3.2 eV)及激发的空穴电子对在迁移过程中易复合等缺点, 导致TiO_2光催化效率较低. 因此, 人们进一步对TiO_2进行改性, 以提高TiO_2的量子收益及其在可见光区域的响应强度. Ananpattarachai等[9]利用溶胶凝胶法制备了N掺杂的TiO_2以及Li等[10]利用直接水解法制备了B掺杂的TiO_2, 结果表明, 利用离子对TiO_2进行掺杂有效降低了禁带宽度. 李晓佩等[11]测试了酞菁改性的介孔TiO_2光催化性能, 结果表明, 染料敏

化后光吸收边红移. 由于多壁碳纳米管(MWCNTs)具有优异的机械性能、导电性、热力学性能及磁性, 人们对MWCNTs/TiO_2开展了广泛的研究工作[12]. Wang等[13]采用溶胶凝胶法制备的MWCNTs-TiO_2进行了光降解苯酚的研究. 杨汉培等[14]采用水热法制备了CNTs-TiO_2, 并考察其光催化降解甲基橙溶液的能力. 目前有关MWCNTs/TiO_2的研究主要集中于光催化剂物理化学性质及催化反应机理, 但应用只局限于液相条件下的苯酚, 甲基橙等, 有关气相污染物尤其是燃煤烟气中NO的光催化脱除还鲜见报道.

本文采用溶胶凝胶法制备了MWCNTs/TiO_2复合型光催化剂, 利用透射电镜(TEM), X射线光电子能谱(XPS), X射线衍射(XRD)及紫外-可见漫反射光谱(UV-Vis)对其进行理化表征; 以模拟燃煤烟气的NO作为目标污染物, 在固定床反应器中对MWCNTs/TiO_2的光催化脱硝性能进行评价, 研究了烟气组分浓度以及MWCNTs的引入对MWCNTs/TiO_2光催化脱硝效率的影响.

2. 实验部分

2.1. MWCNTs/TiO_2的制备

MWCNTs购于中国科学院成都有机化学公司(纯度> 95%, 直径10–20 nm, 长度10–30 μm). 利用混酸法对MWCNTs进行酸化处理, 将1 g MWCNTs超声分散于20 mL浓盐酸及浓硝酸(南京化学试剂有限公司)的混合溶液(H_2SO_4:HNO_3 = 3:1, 体积比), 并用去离子水反复冲洗直至为中性, 置于80 °C的干燥箱中干燥12 h.

将适量酸处理后的MWCNTs超声分散于75 mL无水乙醇(AR, 南京化学试剂有限公司), 25 mL钛酸四丁酯(AR, 南京化学试剂有限公司)及4 mL硝酸的溶液中, 置于磁力搅拌器上持续搅拌, 形成悬浮液. 搅拌1 h后, 将5 mL蒸馏水加入25 mL无水乙醇中, 并调节pH至2, 形成混合液. 将混合液逐滴加入悬浮液中, 陈化凝胶, 80 °C干燥后, 在350–650 °C空气中焙烧3 h. 同上法制备对比样品TiO_2, 只是不添加MWCNTs. 在光催化脱硝实验中, 为了提高MWCNTs/TiO_2与烟气的接触面积, 同时提高光催化剂与烟气的接触时间, 对MWCNTs/TiO_2进行涂覆处理[15]. 制备MWCNTs/TiO_2均匀的浆体, 将适量粒径为2 cm的颗粒状硅胶加入浆体中, 干燥后作为实验用光催化剂颗粒.

2.2. MWCNTs/TiO_2的表征

未酸化及酸化处理的MWCNTs TEM照片采用日本电子公司200 kV场发射透射电镜2100F型进行扫描分析, 测试前将样品超声分散于无水乙醇中, 高倍稀释后附着于铜网(南京中镜科仪技术有限公司). 采用PHI Quantera Ⅱ型X射线光电子能谱仪对样品表面组成进行分析. 采用日本理学公司D/max-2500/PC型阳极转靶X射线衍射仪研究MWCNTs/TiO_2在不同焙烧温度下的晶相及结晶度, 扫描速率为0.02°/s (5°–85°). MWCNTs/TiO_2的UV-Vis光谱利用美国VARIAN公司的紫外/可见光分光光度计进行测定.

2.3. 催化剂的评价

图1为实验系统原理图. 光催化实验在由60 cm长的双层石英管组成的固定床反应器中进行. 内外石英管的直径分别为28和60 mm. 内管用于放置波长为365 nm的高压汞灯, 辐照强度为6.5 W/m^2 (125 W,上海季光特种照明厂). 模拟烟气的成分为0–8% O_2, 0–15% H_2O, 73–508 mg/m^3 NO, 155–1241 mg/m^3 SO_2及平衡气N_2. N_2, O_2, SO_2及NO均来自钢瓶气(南京特种气体有限公司), 通过高精度质量流量计(北京汇博隆有限公司)调节各组分的浓度. N_2分为两路, 一路与NO混合形成主反应气流. 另一路与O_2结合进入水鼓泡器满足反应的湿度要求. 烟气的总体积流量控制在2 L/min, 折合空速为250 h^{-1}). 通过在线测量ECOM烟气分析仪, 可以实时测定NO浓度. 制备的光催化剂对NO有吸附作用, 在开启光源前持续通入NO使得光催化剂达到吸附平衡, 以减少实验结果的偏差. 在光催化脱硝实验中, 紫外光源开启后, 反应时间控制在15 min. 光催化剂的光催化能力以NO的脱除效率进行衡量, NO脱除效率的定义为$R_{NO}=[(NO_{in}-NO_{out})/NO_{in}]\times100\%$, 其中$NO_{in}$为紫外灯开启前NO浓度; NO_{out}为紫外灯关闭时NO浓度.

表1列出了光催化脱硝实验的条件. 工况1研究暗态条件下MWCNTs/TiO_2的吸附性能, 实验开始时, NO首先进入旁路, 浓度达到稳定后, 关闭旁路, NO进入光催化反应器, 测量NO浓度的变化. 工况2研究UV单独光照以及在硅胶, TiO_2和MWCNTs/TiO_2存在下相应的光催化脱硝效率, 建立MWCNTs/TiO_2的基准光催化脱硝效率. 工况3–6研究烟气组分浓度对光催化脱硝效率的影响. 脱硝实验中光催化剂使用量为25 g.

3. 结果与讨论

3.1. 光催化剂形貌

图2(a)为MWCNTs的TEM照片(分辨率100 nm). 可见, 未经酸化处理的MWCNTs发生了聚集, 表面存在部

分无定形碳及其它的杂质, 长度较长, 直径为15–30 nm. 图2(b)酸化处理后MWCNTs的TEM照片(分辨率20 nm). 可以观测到MWCNTs典型的中空结构. 酸化处理后MWCNTs末端开口, 即开端氧化, 同时MWCNTs发生折断, 使得碳纳米管的长度变短; 管壁表面杂质明显减少. 图2(c)为MWCNTs/TiO_2的TEM照片. 由图可见MWCNTs对TiO_2的负载, TiO_2以簇状形式包裹在MWCNTs管壁表面, 其外部直径大于20 nm.

3.2. MWCNTs/TiO_2晶型

图3为500 °C焙烧的TiO_2以及350, 500和650 °C焙烧的MWCNTs/TiO_2的XRD谱. 在350及500 °C焙烧时, TiO_2以锐钛矿相为主, 在25.1° (101)面, 36.9° (103)面, 37.6° (004)面, 38.5° (112)面, 47.9° (200)面, 53.8° (105)面, 55.0° (211)面, 62.6° (204)面和75.1° (215)面分别检测出不同程度的锐钛矿相TiO_2衍射峰. 焙烧温度为500 °C时, TiO_2的(101)面具有更窄的半高峰宽, 表明锐钛矿相结晶度更高; 至650 °C后, TiO_2的晶型由锐钛矿相转变成金红石, 对应的金红石的衍射峰(27.4°)明显增强. 利用分析天平(AUX320, 日本SHIMADZU)对650 °C焙烧的MWCNTs/TiO_2进行精确称量, 发现与500 °C焙烧的MWCNTs/TiO_2(其质量与制备时理论值相近)相比, 有明显质量损失, 说明650 °C焙烧时MWCNTs存在氧化损失. Li等[16]在热重实验中也确认, MWCNTs在550–750 °C温度区间有较大损失. 另外在XRD图谱中未检测出C的衍射峰. Cong等[17]研究发现, MWCNTs的衍射峰位于26.3°, 与锐钛矿(101)面(25.3°)相近, 因而被遮蔽. 将500 °C焙烧的MWCNTs/TiO_2的XRD谱在20°–30°区间(图3插图)进行局部放大, 并未发现可能归于C的衍射肩峰. 这主要是由于MWCNTs含量较少且分布均匀. 另外, 与500 °C焙烧的纯TiO_2相比, 相同温度焙烧的MWCNTs/TiO_2的(101)面衍射峰更加宽泛. 基于Scherrer方程可以估算出MWCNTs/TiO_2与TiO_2的晶粒尺寸分别为11及19.1 nm. 可见, MWCNTs的引入限制了TiO_2晶粒的生长. TEM测得TiO_2平均粒径为15 nm, 大于XRD估算值. Lin等[18]发现XRD估算的为单晶粒径, 而TEM测试中, 晶粒会发生聚集, 单晶聚集成多晶, TEM测得的是单晶及多晶粒径的平均值, 因而偏大. 下文光催化脱硝实验中采用500 °C焙烧的MWCNTs/TiO_2.

3.3. 表面化学成分分析

图4(a)为MWCNTs/TiO_2样品的XPS宽扫图谱, 其C 1*s*, Ti 2*p*及O 1*s*的谱峰对应于C, Ti和O元素. 图4(b)为MWCNTs/TiO_2的C 1*s*窄扫图谱, 对其进行分峰拟合为三个峰. 284.6 eV对应MWCNTs中典型的C=C以及C–C键; 285.9 eV对应C–O键; 287.9 eV处的宽峰对应于C=O键[19]. 图4(c)为MWCNTs/TiO_2的O 1*s*谱, 解叠为530.1, 531.1和532.1 eV三个峰. 其中530.1 eV对应于晶格氧(Ti–O键), 531.1 eV对应于样品表面羟基, 532.1 eV对应于C–O键[17,19]. 从C 1*s*谱中观测到的C–O键以及O 1*s*谱中同时观测到的Ti–O键和C–O键, 可以确认Ti–O–C键的存在. 图4(d) Ti 2*p*的谱中Ti $2p_{1/2}$及Ti $2p_{3/2}$结合能分别为459.1和465.4 eV, 可见Ti^{4+}为主要存在方式. 与纯TiO_2的相比, MWCNTs/TiO_2的Ti 2*p*结合能明显增大, 主要原因为MWCNTs与TiO_2之间Ti–O–C键的存在而引发的电子转移, 改变了Ti离子外部电子云的密度, 导致Ti 2*p*结合能的增加.

3.4. 光催化剂光吸收性质

图5(a)为MWCNTs/TiO_2和TiO_2的UV-Vis谱. TiO_2光吸收边在400 nm附近, 在400–800 nm区域光吸收较弱, 而MWCNTs/TiO_2的光吸收边发生红移现象. 当MWCNTs引入后, 它与TiO_2形成Ti–O–C键, 使得电子发生转移, 从而导致了复合光催化剂的费米能级偏移[20]. 另外, MWCNTs/TiO_2在可见光区域(400–800 nm)具有较强的光吸收, 其原因可能为MWCNTs的电子迁移$\pi \rightarrow \pi^*$及黑色的MWCNTs/TiO_2在可见光区域具有一定的吸收强度[21]. 通过$[F(R)hv]^{1/2}$对hv做曲线($F(R)$为Kubelka-Munk函数, h为普朗克常数, v为光频率)对MWCNTs/TiO_2和TiO_2的禁带宽度进行估算, 分别为2.6和3.0 eV (图5(b)). 由此可见, MWCNTs的引入降低了TiO_2的禁带宽度, 提高了MWCNTs/TiO_2的光利用率.

3.5. 光催化脱硝

3.5.1. 基准曲线

图6为MWCNTs/TiO_2上NO吸附性能. NO在旁路达到平衡后, 浓度稳定在189 mg/m^3. 关闭旁路, 使烟气进入光催化反应器, NO浓度迅速下降, 至3 min时, 达最低, 为162 mg/m^3. 随着涂覆型MWCNTs/TiO_2的吸附饱和, NO浓度逐渐回升, 18 min时接近初始浓度. 可以看出, 涂覆型MWCNTs/TiO_2对NO的吸附效率最高可达到14%.

图7为紫外光照下不同催化剂上的光催化脱硝效率. 可以看出, 仅有紫外光照时, 光催化脱硝过程就可以发生, R_{NO}为16%. 在紫外光照下NO的反应过程与光化学烟雾产生的机理相似, NO氧化形成的NO_2在紫外光照的激发下发生光解形成强氧化性O, 进而O与O_2反应形成强氧化性O_3. 强氧化性物质O及O_3的形成促进了NO的

光化学氧化过程. 相关反应机理[22]如下列反应式所示:

$$NO_2 + h\nu \rightarrow NO + O \quad (1)$$
$$O + O_2 \rightarrow O_3 + O + M \quad (2)$$
$$O_3 + NO \rightarrow NO_2 + O_2 \quad (3)$$
$$O + NO + M \rightarrow NO_2 + M \quad (4)$$
$$O + NO_2 + M \rightarrow NO_3 + M \quad (5)$$
$$O_3 + NO_2 + M \rightarrow NO_3 + O_2 + M \quad (6)$$

光催化脱硝实验中光催化剂堆积形式采用的是MWCNTs/TiO_2涂覆硅胶, 以提高烟气与光催化剂接触面积, 延长反应时间, 因此有必要探究硅胶颗粒单独存在时对光催化脱硝过程的影响. 由图7可见, 在紫外光照条件下, 硅胶颗粒的存在没有促进NO的脱除, R_{NO}反而有所下降. 硅胶具有一定的折射和反射作用, 降低了NO接受UV的能量, 使得R_{NO}微降, 在光催化脱硝实验中硅胶颗粒的影响可以忽略不计.

MWCNTs/TiO_2及TiO_2的R_{NO}分别为46%和35%, 明显高于不含光催化剂时的R_{NO}. 与光化学NO脱除过程相比, 光催化剂存在下的光催化脱除更有利. 光催化剂接受的光子能量超过禁带宽度阀值, 可以形成大量的光生空穴电子对. 空穴电子迁移至光催化剂表面后, 与O_2和H_2O反应后会产生一系列的强氧化自由基O_2^-和·OH等, 从而使NO有效地被氧化, 氧化产物主要生成NO_2, HNO_2和HNO_3. Devahasdin等[23]认为, NO的氧化产物的形成是顺序发生的, 即NO → HNO_2 → NO_2 → HNO_3; 在反应起始阶段, 产物以NO_2和HNO_2为主; 但反应进行到一定阶段, 产物以HNO_3为主, 此时光催化剂表面呈酸性, 则会抑制HNO_2→HNO_3的反应过程. 主要的反应机理[23,24]总结如反应式(7)–(13):

$$TiO_2 + h\nu \rightarrow e^- + h^+ \quad (7)$$
$$h^+ + OH^- \rightarrow \cdot OH \quad (8)$$
$$e^- + O_2 \rightarrow O_2^- \quad (9)$$
$$NO + \cdot OH \rightarrow HNO_2 \quad (10)$$
$$HNO_2 + \cdot OH \rightarrow NO_2 \quad (11)$$
$$NO_2 + \cdot OH \rightarrow NO_3^- \quad (12)$$
$$NO + O_2^- \rightarrow NO_3^- \quad (13)$$

3.5.2. MWCNTs对光催化脱硝的影响

由图7可见, TiO_2为催化剂时R_{NO}仅为35%, 而MWCNTs/TiO_2的R_{NO}可达46%, 其原因有三. 第一, MWCNTs具有优异的导电性能, 可以作为电子快速传输通道[25,26]. TiO_2具有有限的电子转移路径, 而MWCNTs的存在为TiO_2提供了额外的电子迁移轨道, 即通过Ti–O–C转移电子, 延长了电子空穴对的寿命. 第二, MWCNTs的引入抑制了TiO_2晶粒尺寸的生长. Devi等[27]研究表明, 光生空穴电子在迁移过程中的复合主要可分为体复合和面复合, 其中以体复合为主. 具有较小晶粒尺寸的光催化剂可以减少空穴电子迁移到表面的时间, 减少体复合的几率. 第三, MWCNTs的引入使得禁带宽度降低, 因而光利用率更高. 本文采用的紫外光源是以365 nm为主波长的紫外灯, 在400–800 nm区域也有光强存在, MWCNTs/TiO_2禁带宽度的降低使得MWCNTs/TiO_2在相同的辐照强度下可以激发更多的空穴及电子.

3.5.3. 烟气组分对光催化脱硝的影响

图8(a)为NO初始浓度对光催化脱硝效率的影响. 由图可见, 随着NO浓度的增加, 光催化脱硝率从46%逐渐下降至21%, 与Langmuir-Hinshelwood反应动力学原理相符合. 在低浓度NO的条件下, 反应为一级反应; 而高浓度时, 反应为0级, 光催化效率趋于稳定[7]. 燃煤电厂烟气组分中会含有一定浓度的SO_2, 为了探究SO_2对NO脱除效率的影响, 将155–1241 mg/m^3 SO_2注入反应系统. 如图8(b)所示, 当155 mg/m^3的SO_2进入反应系统后, R_{NO}从46%降至39%; 至1241 mg/m^3时, R_{NO}进一步降至29%. Li等[28]研究表明, NO主要吸附于光催化剂表面的羟基基团, 而羟基基团和晶格氧也作为SO_2的吸附位点[29]. NO和SO_2同时进入反应体系后, 对共同吸附位点羟基基团的竞争吸附导致了R_{NO}的下降.

许多研究表明, O_2和H_2O对于光催化氧化过程有重要影响. 图8(c)为O_2浓度对光催化脱硝效率的影响. 在无O_2条件下, R_{NO}仅为17%; 当O_2浓度增加至8%, R_{NO}增至46%. 图8(d)为H_2O浓度对光催化脱硝效率的影响. 在5% H_2O的条件下R_{NO}达到最大值, 为46%; 继续增加H_2O浓度到15%, R_{NO}降至41%. 结果表明, 适当提高H_2O和O_2浓度会促进光催化脱硝过程. 从反应式(8)和(9)可以看出, O_2和H_2O水解形成的羟基分别与迁移至光催化剂表面的光生电子和空穴结合, 形成强氧化性的O_2^-和·OH. O_2及羟基基团在作为电子势阱捕获空穴电子的同时, 促发了反应式(10)–(13), 使得光催化脱硝效率增大[30]. 相对于O_2, H_2O对光催化的影响更受关注. 与O_2^-相比, ·OH具有更强氧化性; 另一方面H_2O对光催化过程具有抑制和促进的双重影响. H_2O能在催化剂表面水解形成的羟基, 不仅可以作为NO和O_2的吸附位点, 而且通过氢键吸附更多的H_2O, 进一步增加羟基基团数量[31], 提高光催化脱硝效率. 赵莉等[8]在研究TiO_2光催化脱硝过程时发现, 当H_2O含量大于6%时, H_2O对光催化脱硝效率有抑制作用, 但其并未给出原因. Henderson[32]研究表明, 光催化剂表面形成的水层会抑制目标降解物进入吸附位点或反应位点, 同样也会抑制O_2进入吸附位点, 从而阻碍了光催化过程的进行. 本文结果表明, H_2O浓度为

0–5%时, 高的H_2O浓度有利于光催化脱硝, 而当H_2O浓度增至15%时, R_{NO}下降至41%, 说明15% H_2O在催化剂表面形成水层, 抑制了分子扩散, 过量的H_2O抑制光催化脱硝. 在反应阶段, H_2O的重要性体现在对光催化产物进行迁移, 抑制光催化剂的失活[33,34]. H_2O促使处于吸附位点吸附态的HNO_2及HNO_3转变为H_2O中溶解态的HNO_2及HNO_3, 吸附态光催化产物的解吸过程实现了光催化剂表面的自清洁, 避免了反应产物对吸附位点的堵塞, 一定程度上抑制了光催化剂的失活.

4. 结论

采用溶胶凝胶法制备了MWCNTs/TiO_2. MWCNTs的引入优化了TiO_2的物理及化学结构. MWCNTs/TiO_2较小的晶粒尺寸, 降低了空穴电子体复合几率. 另一方面, 额外的电子转移通道促使光生电子的快速转移, 促进了空穴电子对的分离. 因而, 与纯TiO_2相比, MWCNTs/TiO_2表现出较好的脱硝性能. 光催化脱硝实验中, 在最佳实验条件(73 mg/m^3 NO, 8% O_2, 5% H_2O)下, 光催化脱硝效率可达46%. 较低的NO初始浓度有助于NO的脱除. 另外, SO_2存在降低了R_{NO}, 原因主要为NO和SO_2对表面有限的吸附及反应位点的竞争吸附; 由于H_2O和O_2能够形成强氧化自由基O_2^-和·OH, 因而对光催化脱硝有促进作用. 而过量H_2O在催化剂表面形成水层抑制光催化脱硝, 实验中15% H_2O促使R_{NO}降低.